Materials Advances

ROYAL SOCIETY OF CHEMISTRY

PAPER

View Article Online
View Journal | View Issue

Cite this: *Mater. Adv.*, 2026, 7, 2416

Tailored magnetic properties in CoFeB–$BiFeO_3$ nanocomposite thin films

Lizabeth Quigley, [a] Nirali A. Bhatt, [a] Katrina Evancho, [a] Jianan Shen, [a] Juanjuan Lu, [a] Claire A. Mihalko, [a] James P. Barnard, [a] Max Chhabra, [a] Ping Lu, [bc] Raktim Sarma, [bc] Aleem Siddiqui [b] and Haiyan Wang *[ad]

Received 9th October 2025,
Accepted 11th January 2026

DOI: 10.1039/d5ma01163a

rsc.li/materials-advances

Ferromagnetic CoFeB (CFB) and multiferroic $BiFeO_3$ (BFO) are both extensively studied materials for thin-film device applications and have previously been implemented in multilayer or bilayer stacks. In this work, we demonstrate, for the first time, particle-in-matrix (PiM) films as a new CFB–BFO nanocomposite form. Two PiM films were deposited under nitrogen or vacuum atmosphere and compared against a more typical bilayer system. The different deposition conditions lead to microstructural tuning of the PiM films, with the two displaying inverted microstructures. The PiM films also displayed a large increase in the saturation magnetization compared to the bilayer film and slightly enhanced antiferromagnetic–ferromagnetic exchange coupling out-of-plane. All three films displayed ferroelectric properties, with the PiM film deposited under a nitrogen atmosphere showing significant leakage. These CFB–BFO nanocomposites present potential for future multiferroic device applications.

Introduction

Novel multiferroic nanocomposite materials enable new applications in devices by combining both ferromagnetic and ferroelectric materials within a single structure, often allowing for stronger properties than either individual material by itself.[1–5] Some applications of these materials include ferroelectric random access memory (FeRAM) and ferroelectric spintronics, depending on which ferromagnetic and ferroelectric materials are selected.[6–11] One ferromagnetic material suited for these applications, among others, is CoFeB (CFB). CFB is a soft ferromagnetic material commonly used in magnetic tunnel junctions (MTJs) for magnetic memory and has a low magnetic damping for spintronic applications.[12–20] While CFB is not ferroelectric, it is metallic in nature and thus conducting, allowing it to work as a charge-conducting layer.[21] For its current applications, CFB is often grown in multilayer stacks, usually with MgO, an insulator that acts as a tunnel barrier in MTJs.[15,16,22–24] Prior work has shown that $BiFeO_3$ (BFO) has emerged as an alternative in tunnel barrier applications with the added bonus of being ferroelectric, allowing this material to work with CFB in future multiferroic applications, particularly FeRAM.[25–31] Due to BFO's low tunneling magnetoresistance as compared to MgO (30% to 600%), tunnel barrier applications of a CFB–BFO system have not been widely considered.[32,33] However, BFO introduces a ferroelectric phase, which MgO cannot because of its insulating nature, allowing for potential regulation of the magnetic states through electric fields. In addition, BFO is a perovskite and is known as one of the single-phase multiferroic materials; it also exhibits weak antiferromagnetic properties.[25,27,28,30] The ferroelectric polarization occurs due to Bi^{3+} in the A site, while the antiferromagnetic properties occur from Fe^{3+} in the B site of the perovskite crystal structure.[25] This provides an advantage for future nanocomposites made of CFB–BFO in the form of antiferromagnetic-ferromagnetic exchange coupling, leading to increased film coercivity when compared to CFB or BFO alone.[34,35] Research has also been done to examine BFO's ability to work in spintronic devices, showing yet again that these two materials are compatible in their future applications.[36]

Conventional designs for multiferroics rely on bilayers or multilayer stacks. The benefit of this layered deposition method is the introduction of lateral interfaces between each of the deposited layers. The in-plane strain introduced by the layers also allows for property tuning of the film by affecting the growth of the next layer.[37] However, this method requires switching between the two different material targets for each new layer to be deposited, increasing deposition time and complexity, especially if done using pulsed laser deposition (PLD). The layered structures are typically achieved through sputter deposition, which is well established for industrial

[a] *School of Materials Engineering, Purdue University, West Lafayette, Indiana 47907, USA. E-mail: hwang00@purdue.edu*
[b] *Sandia National Laboratories, Albuquerque, New Mexico 87185, USA*
[c] *Center for Integrated Nanotechnologies, Sandia National Laboratories, Albuquerque, New Mexico 87185, USA*
[d] *School of Electrical and Computer Engineering, Purdue University, West Lafayette, Indiana 47907, USA*

applications due to its high throughput and deposition area coverage. Also, due to the reliable nature of sputter deposition, most magnetoresistive devices are made with sputtering methods.[38] As an alternative, particle-in-matrix (PiM) nanocomposites, films with nanoparticles of one material embedded within a matrix of another, are co-deposited in a one-step process. PiM films also allow for tunable composition through adjustment of the deposition parameters, further leading to tuned properties.[39,40] There is also an increase in material interfaces in PiM films due to the high surface area of the embedded nanoparticles. The amount of interaction between particles and the matrix depends on the density of the two phases and the size of the nanoparticles, with smaller, more densely spaced nanoparticles having more interactions.[41]

In this work, three CFB–BFO nanocomposite thin films were deposited using PLD: two PiM nanocomposites deposited under different atmospheres (one under a nitrogen partial pressure, the other under vacuum), and a more conventional bilayer film. The bilayer film first had the CFB layer deposited, followed by the BFO layer. The schematics of these three films are shown in Fig. 1A1–A3, and detailed deposition methods can be found in the Experimental section. Previous literature has not reported the deposition of CFB–BFO nanocomposites; thus, this is a novel demonstration of the approach. Reference pure CFB and pure BFO films were also deposited; details can be found in Fig. S2–S4. After deposition, the material and structure of the films were characterized with X-ray diffraction (XRD), transmission electron microscopy (TEM), scanning transmission electron microscopy (STEM) and energy-dispersive X-ray spectroscopy (EDS). The magnetic hysteresis loops (M *vs.* H) and electrical hysteresis loops (P *vs.* E) of each film were then measured to see how the microstructures differed and affected the properties of the films, with the electrical measurement results included in the SI.

Results and discussion

The crystalline phase and orientation of the two particle-in-matrix (PiM) films, deposited under nitrogen and vacuum conditions, were characterized and compared to that of the bilayer film using X-ray diffraction (XRD), as seen in Fig. 1B. Fig. 1A1–A3 show a schematic drawing of each of the deposited films based on the microstructure seen in the transmission electron microscopy (TEM) imaging (see Fig. 2 below). All three films displayed the CoFeB (CFB) (*220*) orientation, showing that this is the preferred texture for CFB growth. Indeed, for the nitrogen PiM film, the CFB (*220*) orientation is the only CFB phase, showing higher growth orientations compared to the two other films with multiple CFB orientations. In the vacuum PiM film, the CFB (*220*) peak has a higher intensity than the other grown CFB orientation, (*020*). The higher CFB phase purity in the nitrogen PiM film may have resulted from the nitrogen partial pressure atmosphere allowing the CFB plasma plume to fully develop, influencing the kinetic energies of the growth. Under vacuum, this effect is minimized, and the plasma plume size is minimized, leading to less optimum CFB growth.

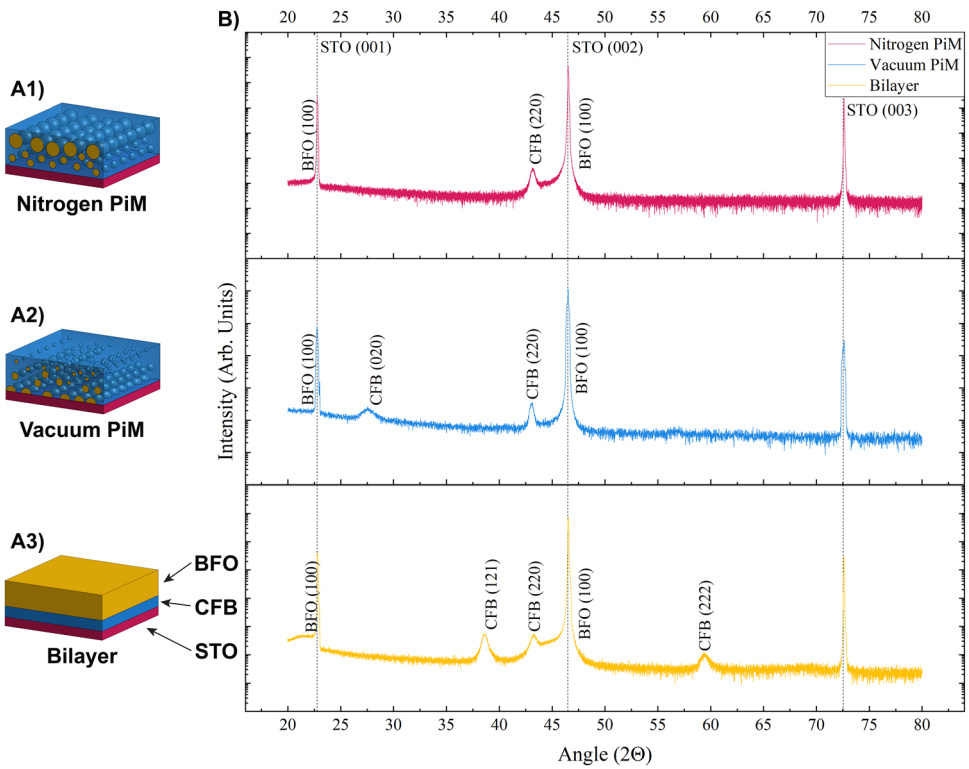

Fig. 1 Schematics for the (A1) nitrogen PiM, (A2) vacuum PiM, and (A3) bilayer films with labeling for the color coding. (B) XRD θ–2θ of the three films.

In the bilayer film, deposited as a more conventional microstructure for direct microstructure and property comparison with the PiM films, multiple CFB phases occurred, despite the deposition also being performed under a nitrogen partial pressure. This would suggest that CFB is not an optimal material to grow directly on STO with PLD, as supported by the growth rate of the material (1.33×10^{-3} nm per pulse) calculated from the bilayer film's growth. The decrease in CFB phases seen in the PiM films suggests that co-deposition with $BiFeO_3$ (BFO) leads to preferential growth of CFB compared to direct growth of CFB by itself on STO. Due to the metallic nature of CFB, it can be assumed that it would grow in an island growth mode, which is further supported by the TEM results shown in Fig. 2, resulting in the multiple orientations seen in the XRD data.[42] In these instances, co-deposition with another material allows for easier growth of these films. For all

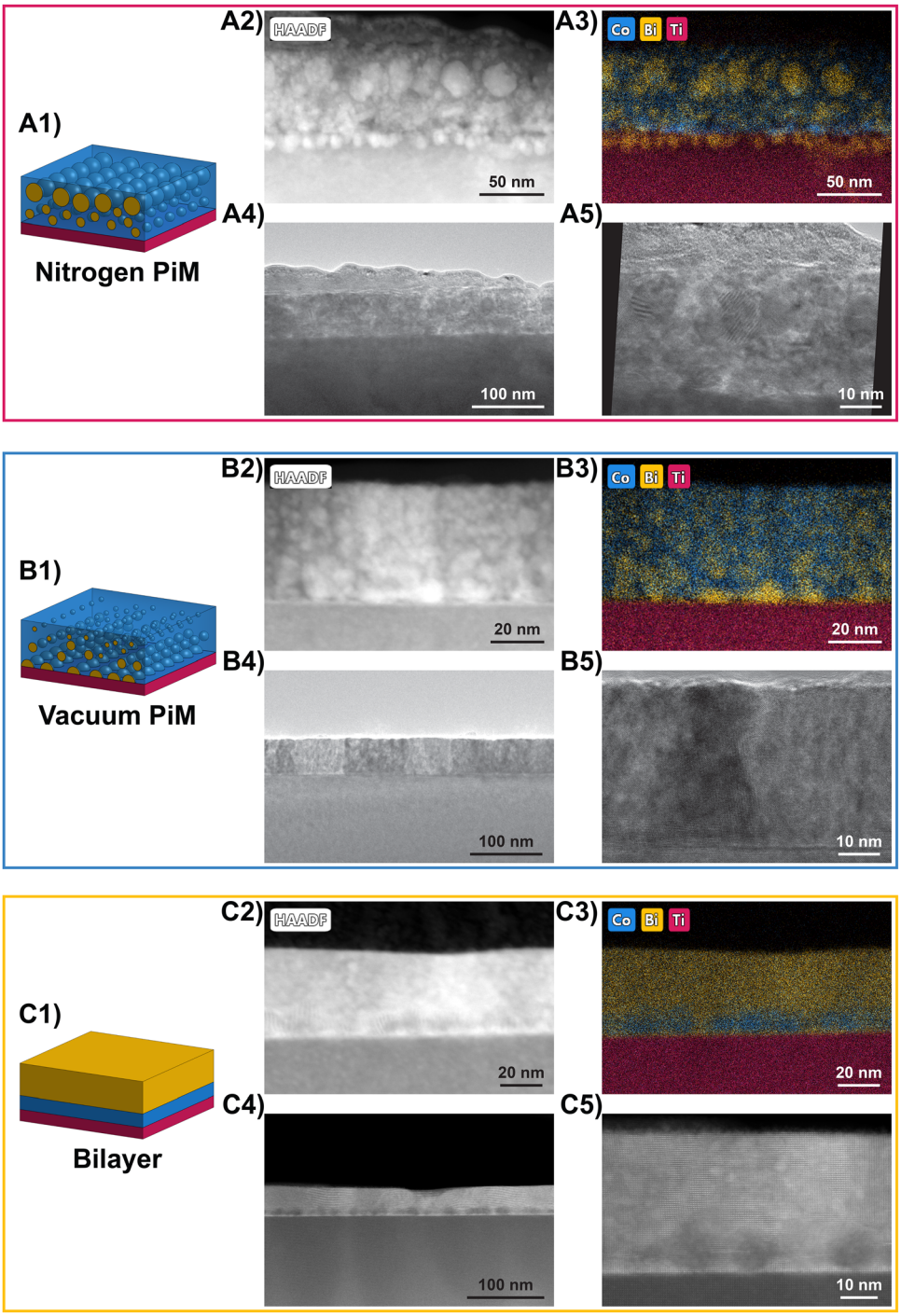

Fig. 2 (A) The nitrogen PiM film, (B) vacuum PiM film, and (C) bilayer film. (1) Schematic drawings, (2) STEM images for the corresponding EDS maps, (3) EDS maps for Co, Bi, and Ti, (4) low-magnification TEM images of the films, and (5) high-resolution images showing the film interface.

three samples, pseudocubic BFO peaks were observed as shoulder peaks on the STO substrate peaks, with no significant differences between the films, showing that the BFO phase grew well under all the deposition conditions. Further analysis of the CFB and BFO phases was performed through in-plane phi scans, as shown in Fig. S1. Scans were conducted in the CFB (*110*) and STO (*110*) orientations, with the STO scan potentially overlapping the BFO phase due to their similar lattice parameters, as seen in Fig. 1. All of the phi scans show the BFO phase with four-fold symmetry, indicating its pseudocubic crystal structure.[28,30] In all three scans, the CFB phase has two wide peaks spanning the width of two STO phi scan peaks, showing a weaker preference for in-plane symmetry than the out-of-plane orientation.

Further microstructural characterization of the films was performed through TEM, scanning transmission electron microscopy (STEM), and energy-dispersive X-ray spectroscopy (EDS) imaging, as shown in Fig. 2. The nitrogen PiM film (Fig. 2A1–A5) shows a film with a preference for large BFO particle growth near the top of the film, though some smaller BFO particles are distributed throughout the lower half of the film, showing that CFB formed as the matrix in these films. This is most apparent from the STEM image and corresponding EDS map in Fig. 2A2 and A3. Despite the preference for BFO particle growth at the top of the film, Fig. 2A3 shows significant amounts of Bi- (shown in yellow) below the substrate because this was the only film to show Bi- diffusion into the STO substrate. A low-magnification TEM image of the film (Fig. 2A4) confirmed that the observed microstructure is uniform across the film and not limited to the area selected for EDS analysis. In the TEM images, an amorphous glue layer is visible at the top of the film, resulting from the preparation of the TEM sample, but examination of the EDS map shows that this is not part of the film. The higher-resolution image in Fig. 2A5 indicates the BFO phases through Moiré patterns, suggesting a misalignment between the CFB and BFO phases under these deposition conditions.

Regarding the Vacuum PiM film (Fig. 2B1–B5), an inverted microstructure relative to the nitrogen PiM film was revealed. As shown in the STEM image and corresponding EDS map in Fig. 2B2 and B3, the larger BFO nanoparticles are more heavily distributed along the substrate, with the smaller nanoparticles distributed in the upper half of the film, and with CFB again forming the matrix. However, the overall distribution of BFO nanoparticles throughout the film is more consistent, with some areas having nanoparticles stacked on top of each other. The low-magnification TEM image (Fig. 2B4) again shows that the microstructure stays consistent throughout the imaged area. Regions of brighter and darker contrast in the STEM image (Fig. 2B2) were attributed to preferential ion milling and not differences in material composition. To ensure this, in the STEM image and corresponding EDS map, both the brighter and darker contrast regions were included, and both exhibit consistent microstructures. Unlike the nitrogen PiM film, the high-resolution image in Fig. 2B5 showed a lack of Moiré patterns, suggesting improved alignment between the CFB and BFO phases.

Finally, the bilayer film (Fig. 2C1–C5), where CFB was deposited first and BFO second, the STEM and corresponding EDS map in Fig. 2C2 and C3 reveal unexpected BFO diffusion through the CFB layer along the STO substrate. This was likely enabled by the discontinuous nature of the CFB layer, allowing for easier diffusion of the BFO phase. However, the uniform thickness of the CFB layer supports some continuity of the CFB layer overall during growth, such as similar surface energies during deposition. The low-magnification image (Fig. 2C4) is used to support the consistency of this microstructure, especially the thin layer of BFO below the CFB layer and the discontinuity of the CFB layer. The last high-resolution image in Fig. 2C5 shows that BFO grows well both above and below the CFB layer. The CFB layer is crystalline in the TEM images, which is also evidenced by its peaks in the XRD in Fig. 1, but this is not as apparent in the TEM image. This difference in crystallinity could help explain the broad peaks seen in the phi scans for the CFB phase in Fig. S1. The O- and Fe- maps for all the films are included in Fig. S5 (the B-map is not included as it is not easily identifiable by EDS). The formation of the CFB

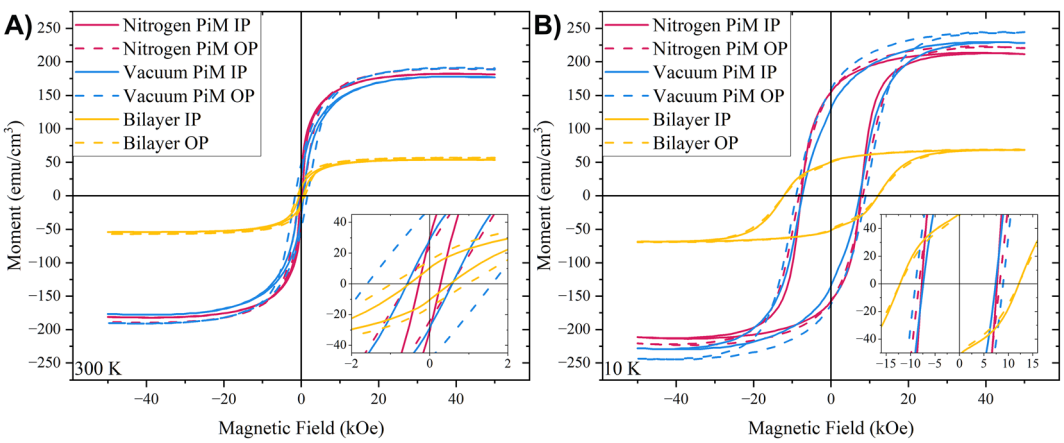

Fig. 3 Magnetic hysteresis (*M vs. H*) data showing both in-plane (IP) and out-of-plane (OP) orientations for all films at (A) 300 K and (B) 10 K, zero-field cooled.

matrix phase for the two PiM films suggests that the co-deposition of the CFB and BFO phases results in better material composition, possibly leading to better magnetic properties due to the increased ferromagnetic CFB phase. Table S1 lists the thickness of all the films, including the Pure CFB and Pure BFO films.

Considering the potential magnetic properties in the films, magnetic hysteresis loops were measured, as shown in Fig. 3. These measurements were performed at both 300 K and 10 K for all three CFB–BFO nanocomposite films. Both PiM films displayed a large increase in saturation magnetization compared to the bilayer film. The saturation magnetization and coercive field for all films and each temperature can be found in Table S2. This includes the values for the Pure CFB and Pure BFO films. The saturation for the pure CFB film is significantly weaker than values commonly seen in the literature, which is a result of the suboptimal CFB deposition seen during the growth on STO through PLD, as shown in the XRD results in Fig. 1. Fig. S4 includes the hysteresis loops for pure BFO and CFB films as references. The PiM films also exhibited stronger out-of-plane (OP) saturation magnetization compared to the in-plane (IP), while the bilayer film had both orientations as equivalent. The orientational preference of the PiM film is attributed to its microstructure, which allows for more anisotropy.[43]

The coercivities of all the films at 300 K were measured to be below 2 kOe, and, in most instances, the bilayer film showed a larger coercivity than the PiM films. One exception is seen in the inset in Fig. 3A, with the OP orientation of the Vacuum PiM film. At 10 K, the bilayer film has the largest coercivity, as seen in the inset in Fig. 3B. The reason for this effect at 300 K is likely due to the microstructure of each film. In the Vacuum PiM film, the distribution of CFB throughout the film thickness enhances the OP magnetic response. In the nitrogen PiM film, the large BFO nanoparticles near the top of the film act almost like the top BFO layer of the bilayer film, minimizing the thickness of the CFB layer. However, the CFB matrix still allows for growth in a three-dimensional manner, allowing for the film's OP coercivity to be larger than its IP coercivity, but not larger than that of the bilayer film. The fact that both PiM films show a preferred OP anisotropy over IP supports their increased anisotropy compared to the bilayer film. This increase in magnetic saturation could also be due to improved growth of the CFB phase and more ferromagnetic CFB in the overall film. Due to the bilayer film having a consistent IP and OP coercivity, it is safe to assume that the increase in the coercivity at 10 K is not due to perpendicular magnetic anisotropy that can occur in other CFB stack systems.[44]

Exchange coupling between the antiferromagnetic BFO and ferromagnetic CFB is expected for the nanocomposite films. To confirm this, magnetic hysteresis loops were measured at 10 K after field cooling (FC) under ±10, ±20, and ±30 kOe. These measurements were performed on all three films in the OP direction (a more detailed explanation is given in the Experimental methods section). The OP orientation was chosen for these measurements to highlight the strength of the nanocomposite design because that previous work, performed with the co-deposited nanocomposite design, has shown a stronger exchange bias in the OP orientation.[45] The resulting hysteresis loops for each measurement can be found in Fig. S6. Fig. 4A shows H_{EB}, the exchange bias field or the shift of the hysteresis loop along the magnetic field axis, for each sample as a result of the applied field during cooling. The corresponding values are listed in Table S3, along with the average coercive field (H_C) and the saturation magnetization. The clear shift seen from the zero-field cooled (ZFC) to the FC states supports the presence of exchange coupling. Another clear indicator of exchange coupling is the negative H_{EB} after positive FC and a positive H_{EB} after negative FC. At an applied cooling field of ±10 kOe, the two PiM films have a larger H_{EB} than the Bilayer film, suggesting that this nanocomposite design enhanced the magnetic interface coupling due to increased surface area between the antiferromagnetic BFO and ferromagnetic CFB. The asymmetry seen between the positive and negative H_{EB} is attributed to incomplete spin relaxation. Measurements were performed in an MPMS3, and were heated to 400 K between measurements, which is insufficient to fully demagnetize the BFO phase with a

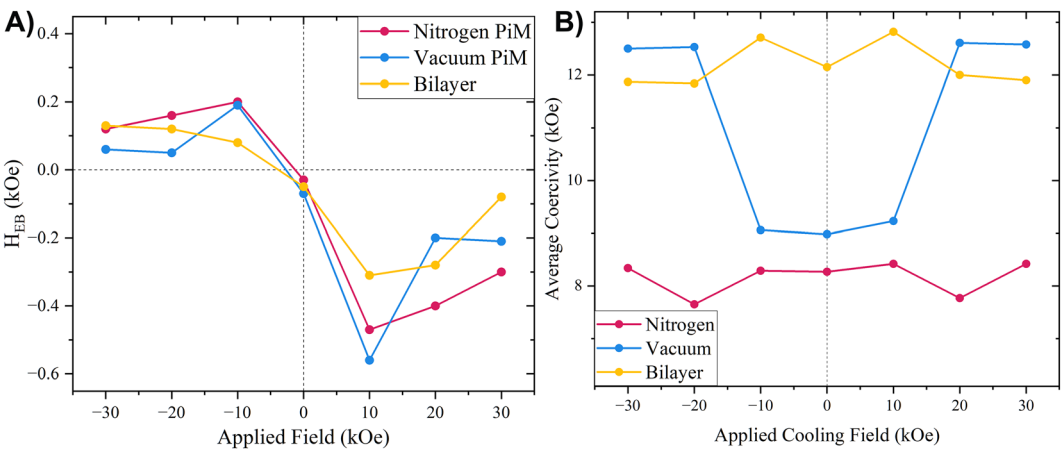

Fig. 4 (A) Graph of H_{EB} *versus* field applied during cooling. (B) The average coercivity for the three films after the zero-field cooled and applied field cooled measurements.

Néel temperature of ~640 K.[27–29,31] As detailed in the experimental methods, the samples were heated to above the Néel temperature between the application of each of the different sets of fields.

When the field-cooled measurements were conducted with the higher applied fields, the bilayer sample did not display the lowest H_{EB}. Instead, the Vacuum PiM film, on average, displayed the lowest exchange bias. However, looking at the hysteresis loops in Fig. S6A–C and the average saturation, graphed in Fig. 4B and listed in Table S3, the saturation magnetization of the sample further increased at the higher applied cooling fields. So, while the exchange bias decreased, the increased saturation of the sample still supports the nanocomposite film experiencing greater AFM-FM exchange coupling than the bilayer film, due to the increased interfaces between CFB and BFO. The nitrogen PiM film does not experience this secondary shift in coercivity but continues to have a greater H_{EB} than the bilayer film, except with the −30 kOe applied cooling field measurement. Due to the H_{EB} values being 0.1 kOe apart from each other, as seen in Table S3, and the negative applied fields experiencing incomplete spin relaxation, this effect can be assumed to be minor, and the nitrogen PiM film experiences overall greater exchange bias than the bilayer film. As seen in Fig. S6D, magnetic moment *versus* temperature measurements (*i.e.*, *M vs. T* curves) were also conducted for these three films to determine whether they showed a ferromagnetic response and whether there were any effects from the suspected oxygen defects in the BFO phase. The measurement temperature range was 8–400 K (exact details of this measurement can be found in the experimental methods). Oxygen vacancies in BFO, and materials like it, can weaken indirect exchange or introduce frustrated or weakly interacting regions, particularly with the Fe–O–Fe bonds, as previously reported.[46] This vacancy-induced magnetic phase softening and spin-glass behavior can be seen in Fig. S6D, supporting the growth of oxygen vacancies in the BFO phase. It can also be seen that these three films' responses follow a pattern based on their film thickness, as reported in Table S1. The Vacuum PiM and bilayer films with comparable thickness exhibit very similar responses in this graph, while the thicker nitrogen PiM has a stronger response at all temperatures.

Considering the possible ferroelectric properties of BFO, polarization–electric field (*P vs. E*) loops, as shown in Fig. S7, were also measured for all three films. All three films exhibited weak polarization, are not fully saturated, and likely do not reach ideal BFO behavior due to the deposition under vacuum or a nitrogen atmosphere. The BFO phases in all three films are likely oxygen-deficient, which leads to lower ferroelectric properties.[31,47,48] Despite this limitation, sufficient ferroelectric BFO is present in each film to produce measurable ferroelectric hysteresis loops. However, due to the discontinuous nature of the BFO phase, there is no clear path for electrical travel through the CFB matrix, or between the BFO and Nb:STO substrate. The nitrogen PiM film, shown in Fig. S7A, has the worst ferroelectric properties due to the occurrence of most leakage, and, as seen in the Fig. S8, this trend continues until measurement failure. All three films show leakage, but the nitrogen PiM film is the worst. This is believed to be due to the microstructure; because the majority of the BFO is congregating towards the top of the film, there is little ferroelectric BFO in contact with either the bottom or top electrode. The Vacuum PiM and bilayer films show better responses, but still no true saturation. Further deposition tuning could be performed to minimize the presence of oxygen vacancies. However, in the two co-deposited microstructures, this would lead to oxidation and degradation of the CFB phase.

Magnetic characterization indicates that the PiM nanocomposite design of the CFB–BFO film offers improved anisotropy when compared to a more traditional bilayer system, although the deposition parameters need to be carefully controlled to avoid compromising the ferroelectric properties. Both PiM films showed an increased magnetic saturation at both room temperature and low temperature, with the coercivities of all films being comparable at room temperature. The PiM films also showed greater exchange coupling than the bilayer film. These enhancements are attributed to the different microstructures in the PiM film, particularly with the BFO nanoparticle arrangement throughout the film. These advantages are achieved through the one-step co-deposition method used for PiM growth, which resulted in better CFB growth when compared to the bilayer film using our PLD deposition parameters. Further tuning of the bilayer deposition parameters could improve this growth, but it would still lack the increased material interfaces from the PiM microstructure. Most importantly, the microstructures of these composite films suggest that this system is sensitive to deposition parameters; *i.e.*, small changes in the deposition parameters can lead to large microstructure changes and significantly affect the properties. On the other hand, this is the first demonstration of the co-growth of CFB- and BFO-based nanocomposites.

Similar BFO-based nanocomposites explored previously include BFO–$CoFe_2O_4$ (CFO), BFO–MgO, and BFO–$MgAl_2O_4$ (MAO), all having been deposited previously to take advantage of BFO's ferroelectric properties with other materials. CFO is one of the most common materials for co-growth due to the capabilities of CFO–BFO films to form new two-phase multiferroic films.[49–52] Given that CFO is a strong ferromagnetic material and BFO is antiferromagnetic, antiferromagnetic-ferromagnetic exchange coupling could still occur in the CFO–BFO system. Future investigations with this new CFB–BFO nanocomposite could include optimizing the ferroelectric properties and testing these materials for their potential in spintronic applications. Further studies on the magnetic damping properties of the CFB–BFO nanocomposites could also be beneficial for future ferroelectric spintronic applications. Another possible direction could be using doped BFO, such as $BiFe_{0.7}Mn_{0.3}O$, which is antiferromagnetic with some internal ferromagnetic domain, possibly allowing for improved coupling.[53] Beyond BFO, other multiferroic materials, especially those with stronger ferroelectric properties, such as $BaFe_{11.9}In_{0.1}O_{19}$ and $BaFe_{12-x}Al_xO_{19}$, could be studied.[54,55] Unfortunately, these mentioned materials are ferromagnetic,

losing out on the AFM–FM exchange coupling present in the CFB–BFO nanocomposite.

Conclusion

This work presents the first experimental demonstration of CoFeB (CFB)–$BiFeO_3$ (BFO) particle-in-matrix (PiM) nanocomposites, which were compared against a more conventional CFB–BFO bilayer film. Two different PiM films were deposited under different deposition conditions, resulting in inverted microstructures, confirming that this material system is sensitive to deposition parameters. The two PiM films showed increased magnetic saturation and a stronger exchange bias compared to the bilayer film, showing the benefit of the PiM microstructure due to the co-deposition of CFB and BFO and allowing for better growth of the CFB phase along with increased material interfaces between CFB and BFO under the growth conditions employed in the PLD experiments. The comparison of the magnetic properties of the bilayer films and PiM is hindered by the fact that the bilayer film was optimized for crystallinity instead of for its magnetic properties. A more extensive study focused on improving deposition parameters on a more common substrate for CoFeB growth, such as Si, could allow a fairer comparison and facilitate future applications by enabling easier device integration. Ferroelectric properties were also observed in all films, despite the obvious leakage due to the oxygen-deficient growth conditions, with further work necessary to improve this characteristic. The combined ferromagnetic and ferroelectric properties suggest that this co-deposition of CFB–BFO PiM nanocomposites has potential for multiple applications ranging from ferroelectric random access memory (FeRAM) to ferroelectric spintronics.

Experimental methods

The BFO ($BiFeO_3$) targets were prepared from bismuth oxide (Bi_2O_3) and iron oxide (Fe_2O_3) powders, pressed into a 2-inch target, and sintered at 700 °C for 10 hours. For the particle in matrix (PiM) depositions, one target was cut into pie-pieces while the other was kept whole. The CFB (CoFeB) target was mixed from Co, Fe, and B powders, and sintered using spark plasma sintering (SPS) at 600 °C for 10 minutes. This was kept whole as it was used as the base of the pie-shaped target. The films were deposited using pulsed laser deposition (PLD) with a KrF excimer laser (Lambda Physik, λ = 248 nm). The nitrogen PiM film was deposited at 550 °C, in an atmosphere of 50 mTorr N_2, with a laser energy of 500 mJ, a laser frequency of 5 Hz, and 5000 pulses. The vacuum PiM film was deposited at 600 °C, under a vacuum atmosphere (at least 3×10^{-6} Torr or lower), with a laser energy of 450 mJ, a laser frequency of 5 Hz, and 5000 pulses. The target used for the two PiM films was a pie-shaped target with a CFB base and BFO pie-pieces on top. The ratio between materials during the deposition was kept consistent at 50 : 50. The bilayer film was deposited at 600 °C, in an atmosphere of 50 mTorr N_2, with a laser energy of 450 mJ, and a laser frequency of 5 Hz, then a deposition pattern of 6000 pulses on the CFB target, followed by 4000 pulses on the BFO target. All films were cooled to room temperature after deposition at 15 °C $minute^{-1}$ in the same atmosphere as the deposition. All films were deposited on $SrTiO_3$ (STO) substrates for XRD, TEM, and magnetic hysteresis measurements, and all films were deposited on Nb:STO substrates as the bottom electrode for electrical hysteresis measurements.

Characterization to confirm the crystallinity and elemental and microstructural qualities of the thin film samples was done with a PANalytical Empyrean XRD with a Cu Kα radiation source and a high-resolution Thermo Fisher Scientific TALOS 200 ×, with TEM and STEM operated at 200 kV. STEM and EDS were performed using a FEI Titan™ G2 80-200 STEM fitted with a Cs probe corrector and ChemiSTEM™ technology (X-FEG™ and SuperX™ energy-dispersive X-ray spectroscopy (EDS) with four windowless silicon drift detectors) at 200 kV. Sample preparation for all samples was done by hand by thinning the sample through manual grinding and polishing. Dimpling and polishing made a thin area in the center of the sample, and the sample preparation was completed with a Gatan PIPS II Model 695 ion miller.

Magnetic hysteresis measurements were completed with an MPMS Model 3 (Quantum Design) with an EverCool SQUID magnetometer at the user facility of the Birck Nanotechnology Center at Purdue University (see birck.research.purdue.edu). The magnetic moment *versus* applied field measurements were completed at both 300 K and 10 K up to a field of ±50 kOe in both the in-plane and out-of-plane directions. To test for antiferromagnetic-ferromagnetic exchange coupling, the sample was cooled to 10 K under an applied field of ±10, ±20, or ±30 kOe. Between each field set (10, 20, and 30 kOe), the sample was heated to above the Néel temperature in a furnace and held there for 30 minutes before cooling to fully relax the spins. In the MPMS 3, before each measurement, the sample was heated to 400 K and kept there for 15 minutes to partially relax the spins, then cooled to 10 K under the selected field. After reaching 10 K, the field was first brought to zero before performing the out-of-plane ±50 kOe hysteresis loop. The field was then brought back to zero, and the sample was returned to room temperature. The positive applied field was measured before the negative applied field of the same strength, *i.e.*, +10 kOe first, then −10 kOe, and the sample was only heated to 400 K between the positive and negative applied fields of the same strength. Corrections for the film thickness (emu cm^{-3}) were done using the full film thickness and not based only on the ferromagnetic CoFeB material thickness. Magnetic moment *versus* temperature measurements were done after the exchange bias measurements, still in the MPMS 3. The samples were heated to 400 K in the MPMS and held there for 30 minutes under zero applied field. They were then cooled to 8 K under zero applied field. The measurement field, 1000 Oe, was then applied, and the sample was heated to 400 K while the ZFC data was collected. The sample was then cooled back to 8 K under the same measurement field while collecting the FC data. The samples were corrected for film

thickness (emu cm^{-3}) in the same manner as in the hysteresis loop, then normalized based on the minimum and maximum measured magnetic moment for each sample.

Ferroelectric hysteresis loops were completed using a Radiant Technologies Precision LC II Ferroelectric Tester. The bottom electrode was Nb:STO, and the top electrode was sputtered platinum with an area of 3×10^{-4} cm^2. The measurement was done with a period of 0.1 ms, and was performed starting at zero, going to the positive drive voltage, back to zero, negative drive voltage, and ending at zero. The measurements were performed in two locations on the samples from 0.1 V until failure in steps of 0.1 V.

Author contributions

Lizabeth Quigley – conceptualization, lead; investigation, lead; methodology, lead; investigation, lead; project administration, lead; validation, lead; visualization, lead; writing – original draft, lead. Nirali A. Bhatt – investigation, supporting. Katrina Evancho – investigation, supporting. Jianan Shen – investigation, supporting. Juanjuan Lu – investigation, supporting. James P. Barnard – investigation, supporting. Max Chhabra – investigation, supporting. Ping Lu – investigation, supporting. Raktim Sarma – supervision, supporting. Aleem Siddiqui – supervision, supporting. Haiyan Wang – funding acquisition, lead; resources, lead; supervision, lead; writing – review & editing, supporting.

Conflicts of interest

There are no conflicts of interest to declare.

Data availability

The data supporting this article have been included as part of the supplementary information (SI). Supplementary information includes corresponding structural and magnetic data for pure CoFeB and $BiFeO_3$ films. For the three samples analyzed in this manuscript, this includes the phi scans, hysteresis loops of the field cooled data, moment *vs.* temperature plot, and electrical data. For all films, tables of the film thickness and magnetic saturation and coercivity. See DOI: https://doi.org/10.1039/d5ma01163a.

Acknowledgements

This work is supported by the U.S. Department of Energy, Office of Science, Basic Energy Sciences under Award No. DE-SC0020077. This work was also partially supported by the Laboratory Directed Research and Development program at Sandia National Laboratories, and is performed, in part, at the Center for Integrated Nanotechnologies, an Office of Science User Facility operated for the U.S. Department of Energy (DOE) Office of Science by Los Alamos National Laboratories and Sandia National Laboratories. Sandia National Laboratories is a multiprogram laboratory managed and operated by National Technology and Engineering Solutions of Sandia, LLC, a wholly owned subsidiary of Honeywell International, Inc., for the U.S. Department of Energy's National Nuclear Security Administration under contract DE-NA0003525. This paper describes objective technical results and analysis. Any subjective views or opinions that might be expressed in the paper do not necessarily represent the views of the U.S. Department of Energy or the United States Government. Additionally, this work was supported by the Sandia National Laboratories Diversity Initiative Fellowship (L. Q. and N. A. B.). The high-resolution STEM work was supported by the U. S. National Science Foundation DMR-2016453. L. Q. also acknowledges the support from the Purdue University Doctoral Graduate Fellowship for the first two years of her PhD study. N. A. B acknowledges the support from the Purdue University Andrews Graduate Fellowship.

References

1 J. Shen, J. P. Barnard and H. Wang, A New Class of Single-Phase Multiferroics: Bismuth-Based Layered Supercell Oxide Thin Films—Current Progress and Future Perspectives, *APL Mater.*, 2024, **12**(4), 040601, DOI: 10.1063/5.0201790.
2 C. Lu, W. Hu, Y. Tian and T. Wu, Multiferroic Oxide Thin Films and Heterostructures, *Appl. Phys. Rev.*, 2015, **2**(2), 021304, DOI: 10.1063/1.4921545.
3 M. M. Vopson, Fundamentals of Multiferroic Materials and Their Possible Applications, *Crit. Rev. Solid State Mater. Sci.*, 2015, **40**(4), 223–250, DOI: 10.1080/10408436.2014.992584.
4 S. Picozzi and C. Ederer, First Principles Studies of Multiferroic Materials, *J. Phys.: Condens. Matter*, 2009, **21**(30), 303201, DOI: 10.1088/0953-8984/21/30/303201.
5 W. Eerenstein, N. D. Mathur and J. F. Scott, Multiferroic and Magnetoelectric Materials, *Nature*, 2006, **442**(7104), 759–765, DOI: 10.1038/nature05023.
6 C.-W. Wu, P.-H. Chen, T.-C. Chang, Y.-F. Tan, S.-K. Lin, Y.-H. Yeh, Y.-C. Zhang, H.-N. Lin, K.-C. Chang, C.-H. Yeh and S. Sze, Phase Transformation on HZO Ferroelectric Layer in Ferroelectric Random-Access Memory Induced by x-Ray Irradiation, *Semicond. Sci. Technol.*, 2024, **39**(2), 025002, DOI: 10.1088/1361-6641/ad1130.
7 N. Nagel, T. Mikolajick, I. Kasko, W. Hartner, M. Moert, C.-U. Pinnow, C. Dehm and C. Mazure, An Overview of FeRAM Technology for High Density Applications, *MRS Proc.*, 2000, **655**, CC1.1.1, DOI: 10.1557/PROC-655-CC1.1.1.
8 D. Takashima, Overview of FeRAMs: Trends and Perspectives, in *2011 11th Annual Non-Volatile Memory Technology Symposium Proceeding*, 2011, pp. 1–6, DOI: 10.1109/NVMTS.2011.6137107.
9 V. Garcia, M. Bibes, L. Bocher, S. Valencia, F. Kronast, A. Crassous, X. Moya, S. Enouz-Vedrenne, A. Gloter, D. Imhoff, C. Deranlot, N. D. Mathur, S. Fusil, K. Bouzehouane and A. Barthélémy, Ferroelectric Control of Spin Polarization, *Science*, 2010, **327**(5969), 1106–1110, DOI: 10.1126/science.1184028.

10 M. Liu, L. Zhang, J. Liu, T. L. Wan, A. Du, Y. Gu and L. Kou, Density Functional Theory Studies on Magnetic Manipulation in NiI2 Layers, *ACS Appl. Electron. Mater.*, 2023, **5**(2), 920–927, DOI: 10.1021/acsaelm.2c01479.

11 Z. Xu, X. Xue, Z. Zhang, B. Mao, R. Li, W. Gao, H. Guo, H. Lu, H. Li and J. Wang, Electrical Control of Spin Polarization in a Multiferroic Heterojunction Based on One-Dimensional Chiral Hybrid Metal Halide, *ACS Nano*, 2025, **19**(12), 12033–12040, DOI: 10.1021/acsnano.4c17686.

12 C. Bilzer, T. Devolder, J.-V. Kim, G. Counil, C. Chappert, S. Cardoso and P. P. Freitas, Study of the Dynamic Magnetic Properties of Soft CoFeB Films, *J. Appl. Phys.*, 2006, **100**(5), 053903, DOI: 10.1063/1.2337165.

13 S. A. Manuilov, A. M. Grishin and M. Munakata, Ferromagnetic Resonance, Magnetic Susceptibility, and Transformation of Domain Structure in CoFeB Film with Growth Induced Anisotropy, *J. Appl. Phys.*, 2011, **109**(8), 083926, DOI: 10.1063/1.3559732.

14 S. U. Jen, Y. D. Yao, Y. T. Chen, J. M. Wu, C. C. Lee, T. L. Tsai and Y. C. Chang, Magnetic and Electrical Properties of Amorphous CoFeB Films, *J. Appl. Phys.*, 2006, **99**(5), 053701, DOI: 10.1063/1.2174113.

15 S. Ikeda, K. Miura, H. Yamamoto, K. Mizunuma, H. D. Gan, M. Endo, S. Kanai, J. Hayakawa, F. Matsukura and H. Ohno, A Perpendicular-Anisotropy CoFeB–MgO Magnetic Tunnel Junction, *Nat. Mater.*, 2010, **9**(9), 721–724, DOI: 10.1038/nmat2804.

16 H. Sato, M. Yamanouchi, K. Miura, S. Ikeda, R. Koizumi, F. Matsukura and H. Ohno, CoFeB Thickness Dependence of Thermal Stability Factor in CoFeB/MgO Perpendicular Magnetic Tunnel Junctions, *IEEE Mag. Lett.*, 2012, **3**, 3000204, DOI: 10.1109/LMAG.2012.2190722.

17 A. S. Silva, S. P. Sá, S. A. Bunyaev, C. Garcia, I. J. Sola, G. N. Kakazei, H. Crespo and D. Navas, Dynamical Behaviour of Ultrathin [CoFeB (tCoFeB)/Pd] Films with Perpendicular Magnetic Anisotropy, *Sci. Rep.*, 2021, **11**(1), 43, DOI: 10.1038/s41598-020-79632-0.

18 A. Gayen, R. Modak, A. Srinivasan, V. V. Srinivasu and P. Alagarsamy, Thickness Dependent Magneto-Static and Magneto-Dynamic Properties of CoFeB Thin Films, *J. Vac. Sci. Technol., A*, 2019, **37**(3), 031513, DOI: 10.1116/1.5091675.

19 E. Gokce Polat, C. Deger and F. Yildiz, Investigation of Ferromagnetic Resonance and Damping Properties of CoFeB, *Curr. Appl. Phys.*, 2019, **19**(5), 614–620, DOI: 10.1016/j.cap.2019.03.002.

20 S. Nayak, S. Mohanty, B. Bhusan Singh and S. Bedanta, Magnetic Properties in Soft (CoFeB)/Hard (Co) Bilayers Deposited under Different Ar Gas Pressure, *J. Phys.: Condens. Matter*, 2022, **34**(38), 385801, DOI: 10.1088/1361-648X/ac7f72.

21 Y. Han, J. Han, H. J. Choi, H.-J. Shin and J. Hong, Microscopic and Electronic Roles of B in CoFeB-Based Magnetic Tunnel Junctions, *J. Mater. Chem.*, 2011, **21**(38), 14967–14970, DOI: 10.1039/C1JM12096D.

22 H. Liu, X. Mao, J. Cui, S. Jiang and W. Zhang, Investigation of High Temperature Electrical Insulation Property of MgO Ceramic Films and the Influence of Annealing Process, *Ceram. Int.*, 2019, **45**(18, Part A), 24343–24347, DOI: 10.1016/j.ceramint.2019.08.151.

23 T. Yamamoto, T. Ichinose, J. Uzuhashi, T. Nozaki, T. Ohkubo, K. Yakushiji, S. Tamaru, H. Kubota, A. Fukushima, K. Hono and S. Yuasa, Perpendicular Magnetic Anisotropy and Its Voltage Control in MgO/CoFeB/Mo/CoFeB/MgO Junctions, *J. Phys. D: Appl. Phys.*, 2022, **55**(27), 275003, DOI: 10.1088/1361-6463/ac6634.

24 G.-G. An, J.-B. Lee, S.-M. Yang, J.-H. Kim, W.-S. Chung and J.-P. Hong, Highly Stable Perpendicular Magnetic Anisotropies of CoFeB/MgO Frames Employing W Buffer and Capping Layers, *Acta Mater.*, 2015, **87**, 259–265, DOI: 10.1016/j.actamat.2015.01.022.

25 G. Catalan and J. F. Scott, Physics and Applications of Bismuth Ferrite, *Adv. Mater.*, 2009, **21**(24), 2463–2485, DOI: 10.1002/adma.200802849.

26 H. Sun, Z. Luo, C. Liu, C. Ma, Z. Wang, Y. Yin and X. Li, A Flexible BiFeO3-Based Ferroelectric Tunnel Junction Memristor for Neuromorphic Computing, *J. Materiomics*, 2022, **8**(1), 144–149, DOI: 10.1016/j.jmat.2021.04.009.

27 H. Ishiwara, Impurity Substitution Effects in BiFeO3 Thin Films—From a Viewpoint of FeRAM Applications, *Curr. Appl. Phys.*, 2012, **12**(3), 603–611, DOI: 10.1016/j.cap.2011.12.019.

28 D. Sando, A. Barthélémy and M. Bibes, BiFeO3 Epitaxial Thin Films and Devices: Past, Present and Future, *J. Phys.: Condens. Matter*, 2014, **26**(47), 473201, DOI: 10.1088/0953-8984/26/47/473201.

29 A. Singh, Z. R. Khan, P. M. Vilarinho, V. Gupta and R. S. Katiyar, Influence of Thickness on Optical and Structural Properties of BiFeO3 Thin Films: PLD Grown, *Mater. Res. Bull.*, 2014, **49**, 531–536, DOI: 10.1016/j.materresbull.2013.08.050.

30 M. Botea, C. Chirila, G. A. Boni, I. Pasuk, L. Trupina, I. Pintilie, L. M. Hrib, B. Nicu and L. Pintilie, Lead-Free BiFeO3 Thin Film: Ferroelectric and Pyroelectric Properties, *Electron. Mater.*, 2022, **3**(2), 173–184, DOI: 10.3390/electronicmat3020015.

31 K. Y. Yun, M. Noda, M. Okuyama, H. Saeki, H. Tabata and K. Saito, Structural and Multiferroic Properties of BiFeO3 Thin Films at Room Temperature, *J. Appl. Phys.*, 2004, **96**(6), 3399–3403, DOI: 10.1063/1.1775045.

32 H. Béa, M. Bibes, S. Cherifi, F. Nolting, B. Warot-Fonrose, S. Fusil, G. Herranz, C. Deranlot, E. Jacquet, K. Bouzehouane and A. Barthélémy, Tunnel Magnetoresistance and Robust Room Temperature Exchange Bias with Multiferroic $BiFeO_3$ Epitaxial Thin Films, *Appl. Phys. Lett.*, 2006, **89**(24), 242114, DOI: 10.1063/1.2402204.

33 S. Ikeda, J. Hayakawa, Y. Ashizawa, Y. M. Lee, K. Miura, H. Hasegawa, M. Tsunoda, F. Matsukura and H. Ohno, Tunnel Magnetoresistance of 604% at 300K by Suppression of Ta Diffusion in CoFeB/MgO/CoFeB Pseudo-Spin-Valves Annealed at High Temperature, *Appl. Phys. Lett.*, 2008, **93**(8), 082508, DOI: 10.1063/1.2976435.

34 X. Martí, B. G. Park, J. Wunderlich, H. Reichlová, Y. Kurosaki, M. Yamada, H. Yamamoto, A. Nishide,

J. Hayakawa, H. Takahashi and T. Jungwirth, Electrical Measurement of Antiferromagnetic Moments in Exchange-Coupled IrMn/NiFe Stacks, *Phys. Rev. Lett.*, 2012, **108**(1), 017201, DOI: 10.1103/PhysRevLett.108.017201.

35 B. Skubic, J. Hellsvik, L. Nordström and O. Eriksson, Exchange Coupling and Exchange Bias in FM/AFM Bilayers for a Fully Compensated AFM Interface, *Acta Phys. Pol., A*, 2009, **115**(10), 25–29.

36 S. M. Yakout, Spintronics and Innovative Memory Devices: A Review on Advances in Magnetoelectric BiFeO3, *J. Supercond. Nov. Magn.*, 2021, **34**(2), 317–338, DOI: 10.1007/s10948-020-05764-z.

37 J. Shah, P. Bhatt, K. Diana Diana Dayas and R. K. Kotnala, Significant Role of Antiferromagnetic $GdFeO_3$ on Multiferroism of Bilayer Thin Films, *Mater. Res. Express*, 2018, **5**(2), 026416, DOI: 10.1088/2053-1591/aaab8e.

38 J. E. Greene, Review Article: Tracing the Recorded History of Thin-Film Sputter Deposition: From the 1800s to 2017, *J. Vac. Sci. Technol., A*, 2017, **35**(5), 05C204, DOI: 10.1116/1.4998940.

39 K. Balázsi and C. Balázsi, Application of Sputtered Ceramic TiC/a:C Thin Films with Different Structures by Changing the Deposition Parameters, *Int. J. Appl. Ceram. Technol.*, 2022, **19**(2), 753–761, DOI: 10.1111/ijac.13941.

40 S. Misra, L. Li, J. Jian, J. Huang, X. Wang, D. Zemlyanov, J.-W. Jang, F. H. Ribeiro and H. Wang, Tailorable Au Nanoparticles Embedded in Epitaxial TiO_2 Thin Films for Tunable Optical Properties, *ACS Appl. Mater. Interfaces*, 2018, **10**(38), 32895–32902, DOI: 10.1021/acsami.8b12210.

41 S. J. Gilbert, M. P. McGarry, M. L. Meyerson, P. G. Kotula, L. Yates, J. A. Ohlhausen, P. A. Sharma, A. Trofe, M. P. Siegal and L. B. Biedermann, Structural, Chemical, and Electronic Control in Co–SiNx Granular Metals for High-Pass Filter Applications, *J. Appl. Phys.*, 2025, **137**(6), 065101, DOI: 10.1063/5.0238917.

42 J. Song and H. Wang, A Material Design Guideline for Self-Assembled Vertically Aligned Nanocomposite Thin Films, *J. Phys. Mater.*, 2025, **8**(1), 012002, DOI: 10.1088/2515-7639/ad9bee.

43 A. Tamion, C. Raufast, M. Hillenkamp, E. Bonet, J. Jouanguy, B. Canut, E. Bernstein, O. Boisron, W. Wernsdorfer and V. Dupuis, Magnetic Anisotropy of Embedded Co Nanoparticles: Influence of the Surrounding Matrix, *Phys. Rev. B:Condens. Matter Mater. Phys.*, 2010, **81**(14), 144403, DOI: 10.1103/PhysRevB.81.144403.

44 M. Yamanouchi, A. Jander, P. Dhagat, S. Ikeda, F. Matsukura and H. Ohno, Domain Structure in CoFeB Thin Films With Perpendicular Magnetic Anisotropy, *IEEE Mag. Lett.*, 2011, **2**, 3000304, DOI: 10.1109/LMAG.2011.2159484.

45 J. Huang, A. Gellatly, A. Kauffmann, X. Sun and H. Wang, Exchange Bias Effect along Vertical Interfaces in $La_{0.7}Sr_{0.3}MnO_3$:NiO Vertically Aligned Nanocomposite Thin Films Integrated on Silicon Substrates, *Cryst. Growth Des.*, 2018, **18**(8), 4388–4394, DOI: 10.1021/acs.cgd.8b00366.

46 S. V. Trukhanov, A. V. Trukhanov, A. N. Vasiliev, A. M. Balagurov and H. Szymczak, Magnetic State of the Structural Separated Anion-Deficient $La_{0.70}Sr_{0.30}MnO_{2.85}$ Manganite, *J. Exp. Theor. Phys.*, 2011, **113**(5), 819–825, DOI: 10.1134/S1063776111130127.

47 J. F. Scott, Ferroelectrics Go Bananas, *J. Phys.: Condens. Matter*, 2007, **20**(2), 021001, DOI: 10.1088/0953-8984/20/02/021001.

48 S. V. Trukhanov, A. V. Trukhanov, A. N. Vasiliev and H. Szymczak, Frustrated Exchange Interactions Formation at Low Temperatures and High Hydrostatic Pressures in $La_{0.70}Sr_{0.30}MnO_{2.85}$, *J. Exp. Theor. Phys.*, 2010, **111**(2), 209–214, DOI: 10.1134/S106377611008008X.

49 R. Comes, H. Liu, M. Khokhlov, R. Kasica, J. Lu and S. A. Wolf, Directed Self-Assembly of Epitaxial $CoFe_2O_4$–$BiFeO_3$ Multiferroic Nanocomposites, *Nano Lett.*, 2012, **12**(5), 2367–2373, DOI: 10.1021/nl3003396.

50 W. Salamon, L. Gondek, J. Kanak, M. Sikora, J. Pawlak, M. Szuwarzyński, P. A. Krawczyk, M. Perzanowski, K. Maćkosz and A. Żywczak, Self-Assembled Epitaxial $BiFeO_3$ Nanostructures as a Tailored Platform for Vertically Aligned Nanocomposites Development, *Appl. Surf. Sci.*, 2023, **607**, 154928, DOI: 10.1016/j.apsusc.2022.154928.

51 Z. Wang, Y. Li, R. Viswan, B. Hu, V. G. Harris, J. Li and D. Viehland, Engineered Magnetic Shape Anisotropy in $BiFeO_3$–$CoFe_2O_4$ Self-Assembled Thin Films, *ACS Nano*, 2013, **7**(4), 3447–3456, DOI: 10.1021/nn4003506.

52 D. H. Kim, X. Sun, T. C. Kim, Y. J. Eun, T. Lee, S. G. Jeong and C. A. Ross, Magnetic Phase Formation in Self-Assembled Epitaxial $BiFeO_3$–MgO and $BiFeO_3$–$MgAl_2O_4$ Nanocomposite Films Grown by Combinatorial Pulsed Laser Deposition, *ACS Appl. Mater. Interfaces*, 2016, **8**(4), 2673–2679, DOI: 10.1021/acsami.5b10676.

53 D. V. Karpinsky, M. V. Silibin, S. I. Latushka, D. V. Zhaludkevich, V. V. Sikolenko, R. Svetogorov, M. I. Sayyed, N. Almousa, A. Trukhanov, S. Trukhanov and A. A. Belik, Temperature-Driven Transformation of the Crystal and Magnetic Structures of $BiFe_{0.7}Mn_{0.3}O_3$ Ceramics, *Nanomaterials*, 2022, **12**(16), 2813, DOI: 10.3390/nano12162813.

54 F. G. Agayev, S. V. Trukhanov, A. V. Trukhanov, S. H. Jabarov, G. S. Ayyubova, M. N. Mirzayev, E. L. Trukhanova, D. A. Vinnik, A. L. Kozlovskiy, M. V. Zdorovets, A. S. B. Sombra, D. Zhou, R. B. Jotania, C. Singh and A. V. Trukhanov, Study of Structural Features and Thermal Properties of Barium Hexaferrite upon Indium Doping, *J. Therm. Anal. Calorim.*, 2022, **147**(24), 14107–14114, DOI: 10.1007/s10973-022-11742-5.

55 A. V. Trukhanov, S. V. Trukhanov, V. G. Kostishin, L. V. Panina, M. M. Salem, I. S. Kazakevich, V. A. Turchenko, V. V. Kochervinskii and D. A. Krivchenya, Multiferroic Properties and Structural Features of M-Type Al-Substituted Barium Hexaferrites, *Phys. Solid State*, 2017, **59**(4), 737–745, DOI: 10.1134/S1063783417040308.